Electronic Supplementary Material (ESI) for Journal of Materials Chemistry B.

Supporting Information

The synergistic effect of Co/Ni in ultrathin metal-organic frameworks nanosheets for the Prominent Optimization of non-enzymatic electrochemical glucose detection

Haihan Zou, Dongyan Tian, Chao Lv, Songmei Wu, Guanxuan Lu, Yifan Guo, Yubin Liu, Yu Yu, and Kejian Ding**

School of Science, Beijing Jiaotong University, Beijing 100044, P.R. China.

E-mail: dkjian@bjtu.edu.cn; yuyu@bjtu.edu.cn

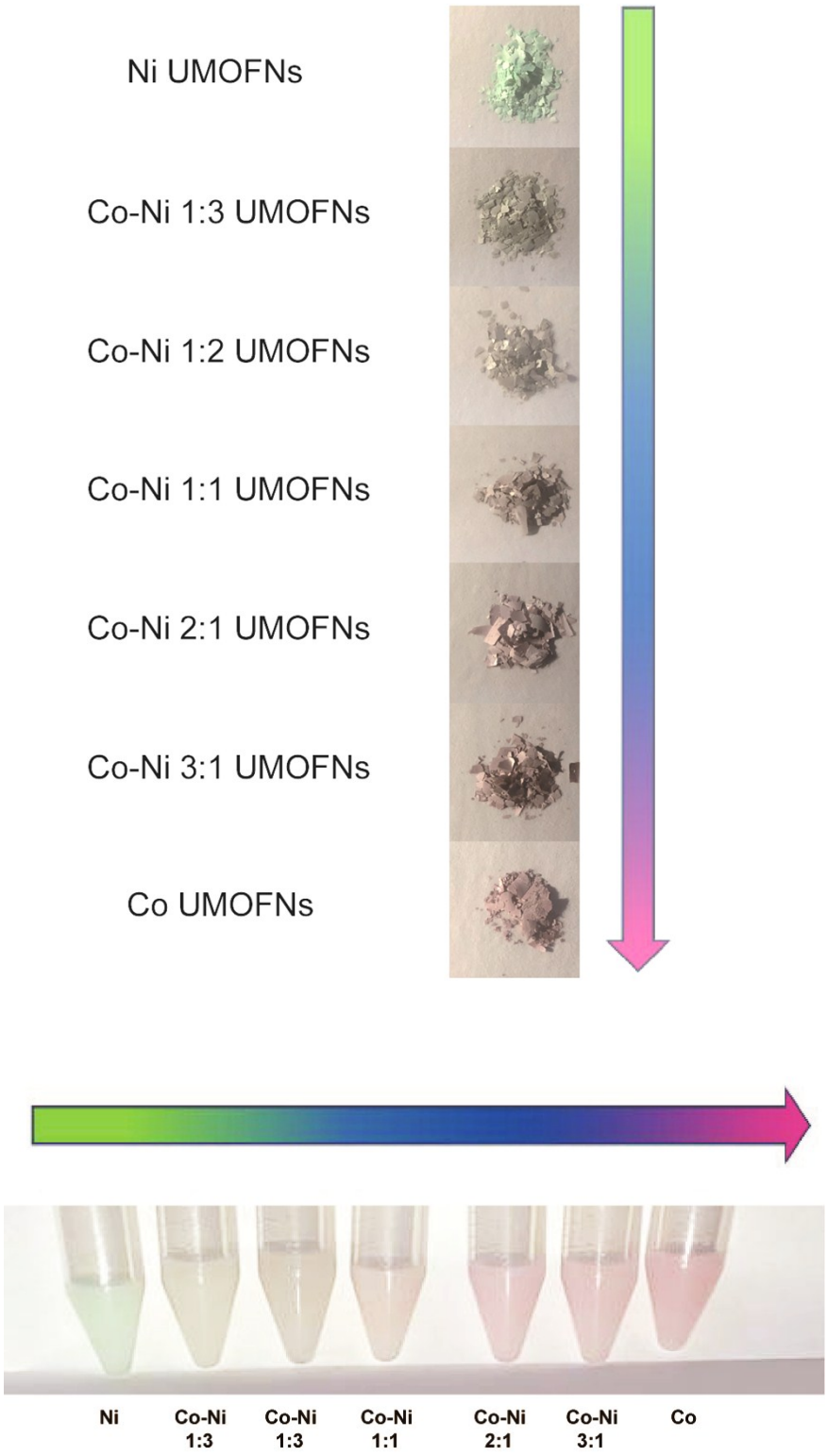

Figure S1. Photos of UMOFNs powder with seven different Co/Ni ratios (color gradually changed from green to purple as the Co ratio increase).

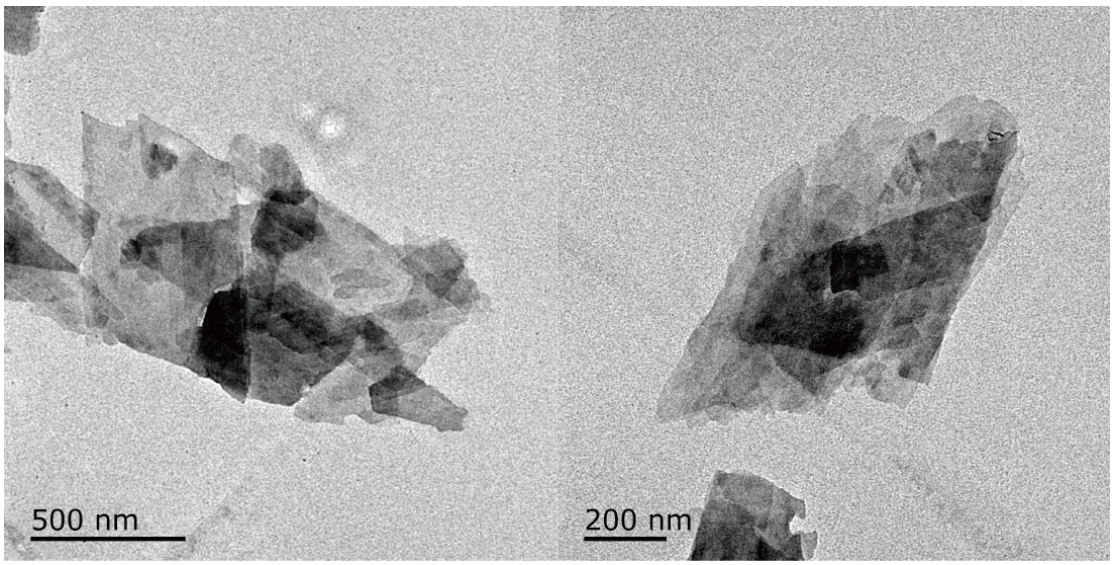

Figure S2. TEM images of Co-Ni 2:1 UMOFNs in different scaling.

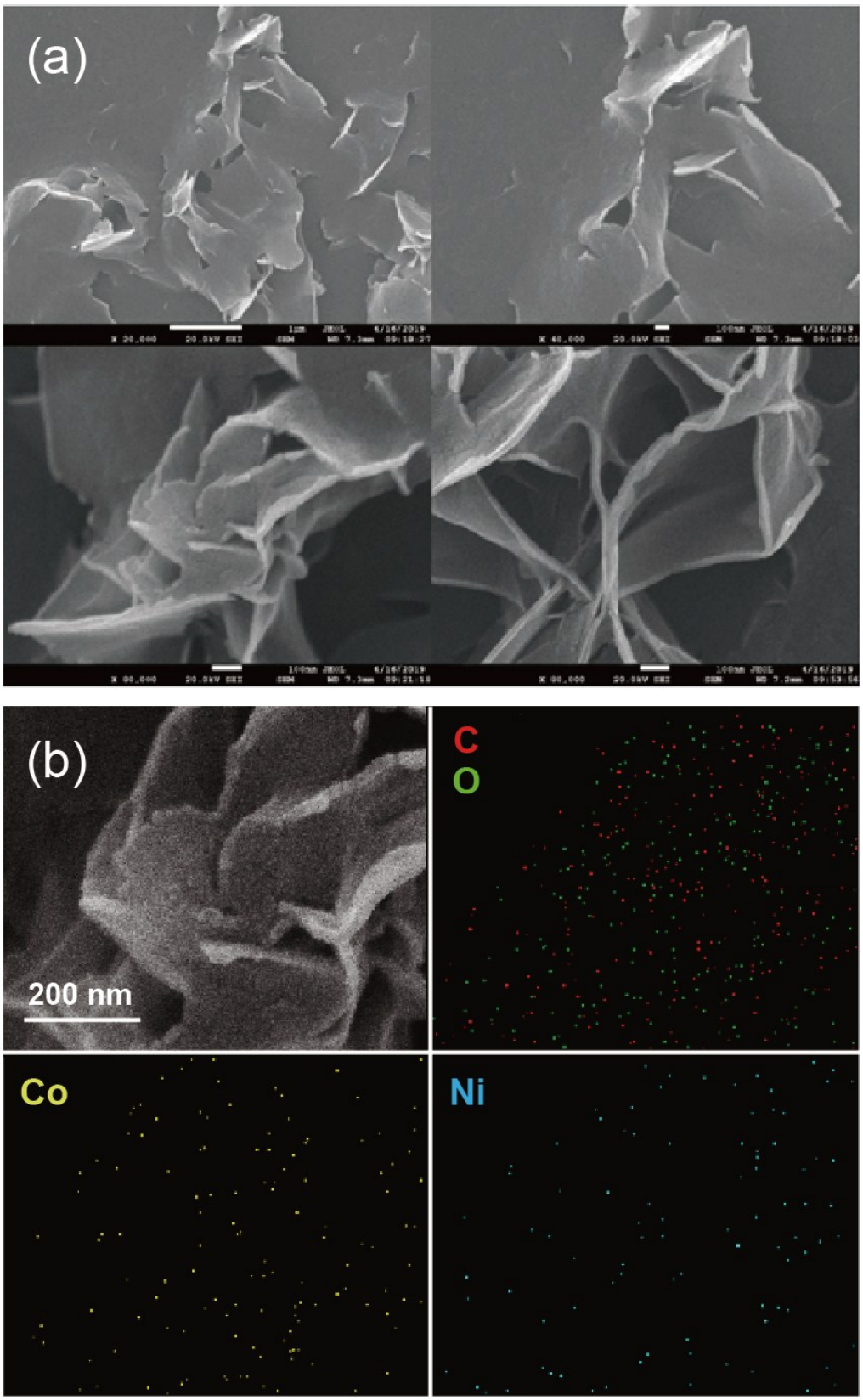

Figure S3. (a) SEM images of Co-Ni 2:1 UMOFNs in different scaling. (b) SEM image and SEM-EDS elements distribution (C, O, Co, Ni) mapping images of Co-Ni 2:1 UMOFNs.

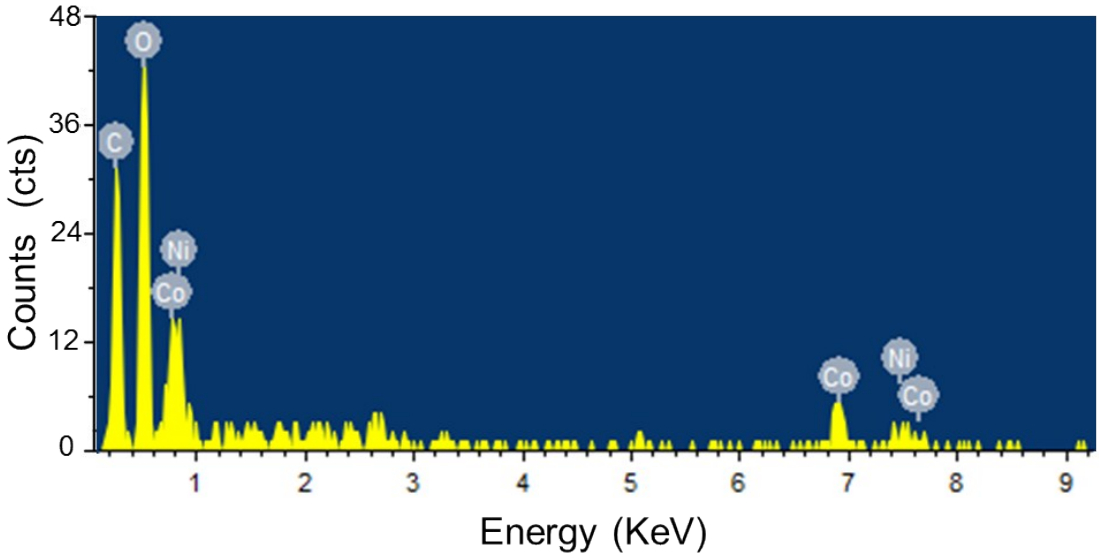

Figure S4. SEM-EDS results of Co-Ni 2:1 UMOFNs.

Table S1. (a) Elemental composition (%) of elements C, O, Co and Ni UMOFNs in seven different Co/Ni ratios UMOFNs materials (SEM-EDS). (b) the comparison of elemental composition (%) of elements C, O, Co and Ni (Co-Ni 2:1 UMOFNs) and Co/Ni atomic ratios by different technologies (SEM-EDS, XPS).

(a)	Elements (atomic %)				
Sample.	**C**	**O**	**Co**	**Ni**	**Co/Ni ratio**
Co UMOFNs	53.62	44.34	2.04	\	\
Co-Ni 3:1 UMOFNs	51.15	46.89	1.52	0.44	3.45
Co-Ni 2:1 UMOFNs	48.55	49.01	1.70	0.75	2.26
Co-Ni 1:1 UMOFNs	50.72	46.95	1.12	1.20	0.93
Co-Ni 1:2 UMOFNs	50.62	47.38	0.70	1.30	0.53
Co-Ni 1:3 UMOFNs	47.50	49.88	0.74	1.88	0.39
Ni UMOFNs	48.61	49.23	\	2.16	\

(b)	Elements (atomic %)				
Method	**C**	**O**	**Co**	**Ni**	**Co/Ni ratio**
SEM-EDS	48.55	49.01	1.70	0.75	2.26
XPS	57.43	32.67	6.50	3.41	1.89

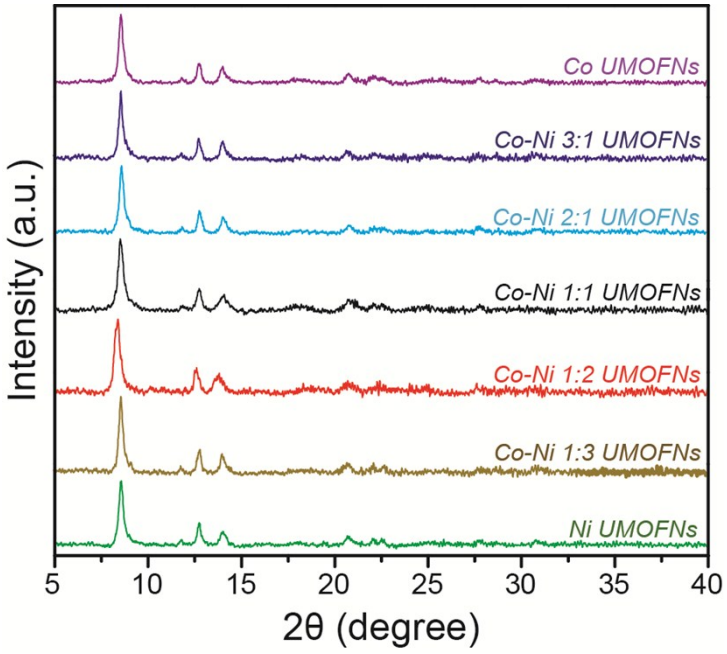

Figure S5. XRD patterns of UMOFNs with seven different Co/Ni ratios. The result directly reflects the compounds are the same crystal phase.

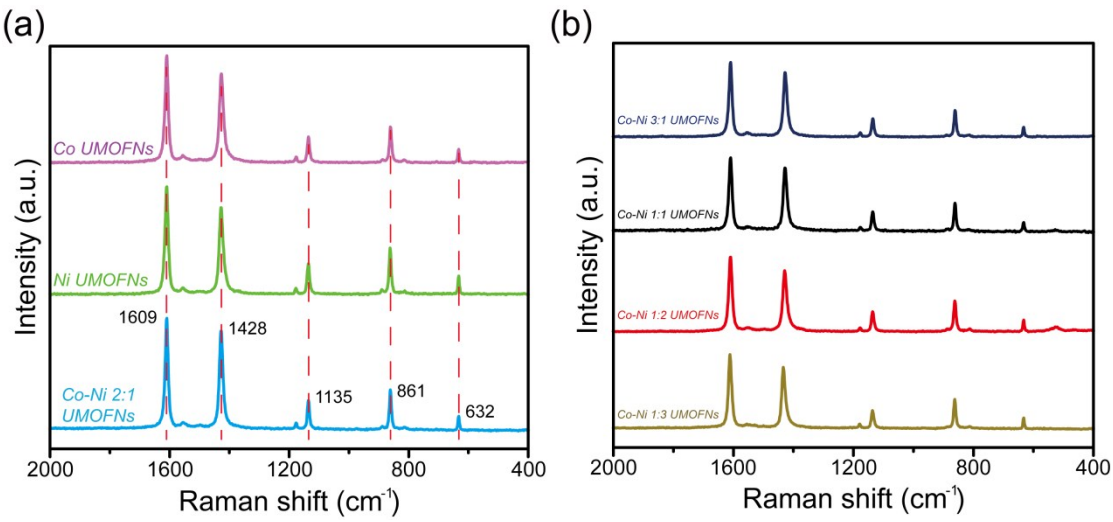

Figure S6. Raman spectra of UMOFNs with seven different Co/Ni ratios.

All materials showed the same band distribution in Raman spectra. From 2000 to 620 cm-1, the vibration of the terephthalic acid part was dominant in the Raman spectral band of UMOFNs.[S1] The band at 1609 cm^{-1} belongs to the C=C stretching vibration of benzene. The band at 1428 cm^{-1} belongs to the carboxyl symmetric stretching vibration, and the band at 1135 cm^{-1} belongs to the C-C stretching vibration of a functional group. The 861 cm^{-1} and 632 cm^{-1} bands belong to the in-plane deformation vibration of the C-H functional group. Raman spectrum reflected the complete existence of the terephthalic acid part in the material, which also confirms the success of the UMOFNs synthesis.

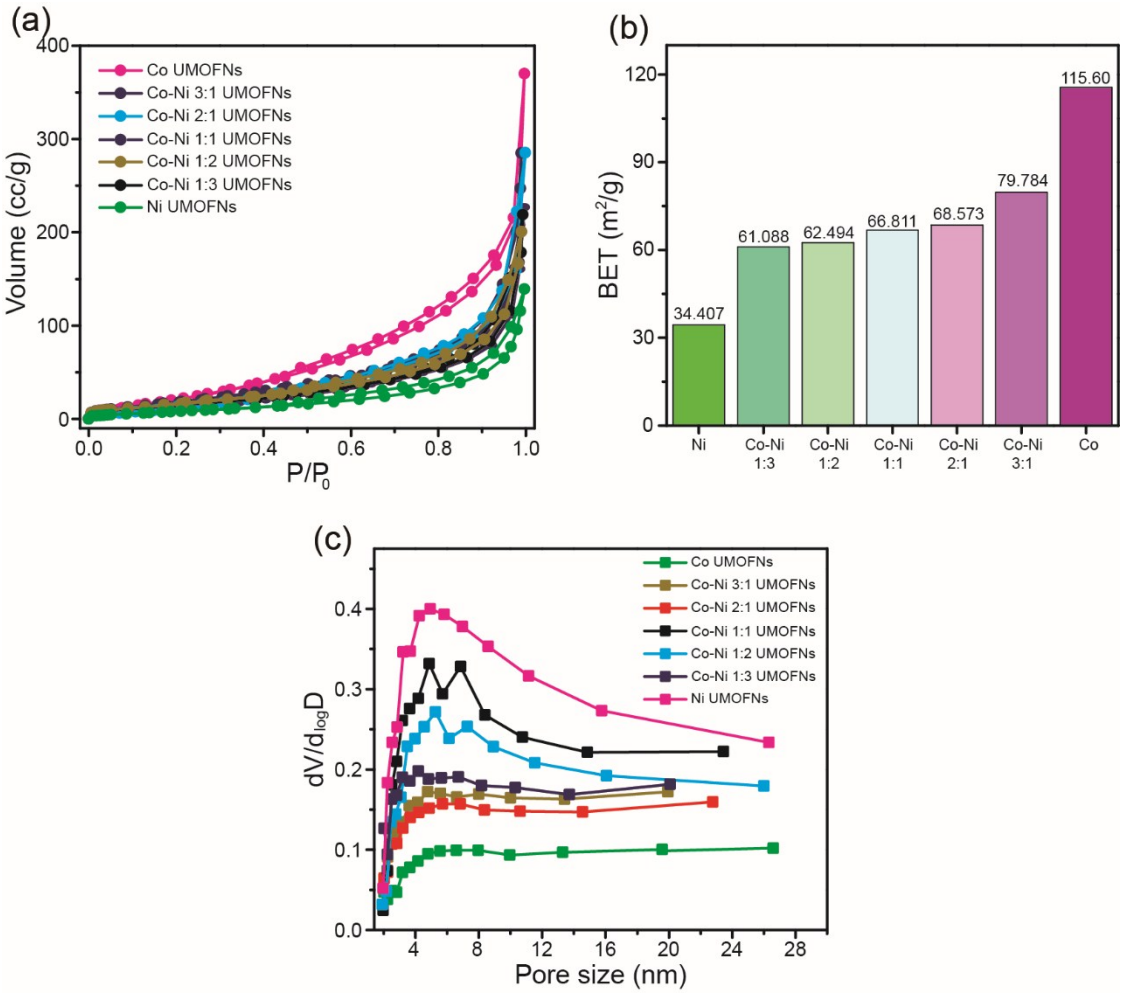

Figure S7. (a) N_2 adsorption-desorption isotherm of UMOFNs in seven different Co/Ni ratios. (b) The value of Brunauer-Emmett-Teller (BET) of UMOFNs in seven different Co/Ni ratios. (c) Pore size distribution profiles of seven different Co/Ni ratios in UMOFNs.

N_2 isothermal adsorption and deposition curves of Co-Ni 2:1 UMOFNs at 77k can be considered as type II with small H4 hysteretic loop, and obtained 68.573 m^2/g Brunauer-Emmett-Teller (BET) surface values, which should be related with the slit-like mesopores (without microporous sorption) formed by aggregation of nanosheets.[S2] This result is also in consistent with the compact packing crystallographic nature of Co/Ni UMOFNs. Compared with Ni UMOFNs, the Brunauer-Emmett-Teller (BET) surface value was increased with the rise of Co doping ratio due to the material aggregation (Figure S7b), so Co element plays a critical role for the increase of UMOFNs surface area. Furthermore, Pore size distribution which was calculated by BJH method[S3] finding that the materials were

centered at 4 - 10 nm (Figure S7c). Relatively large specific surface area lead to better mass tranfer efficiency and high active site exposure, which may play a crucial role in electrochemical non-enzymatic glucose sensing performance improvement.

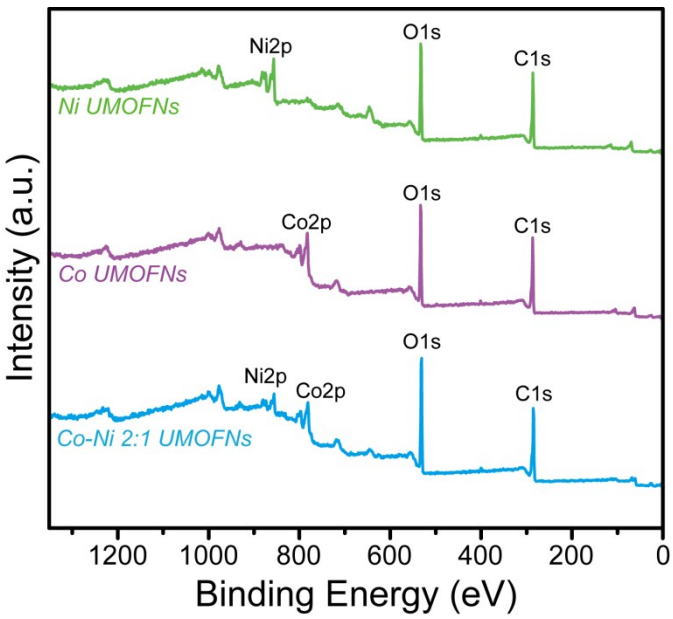

Figure S8. XPS survey spectra of Co-Ni 2:1 UMOFNs, Co UMOFNs and Ni UMOFNs.

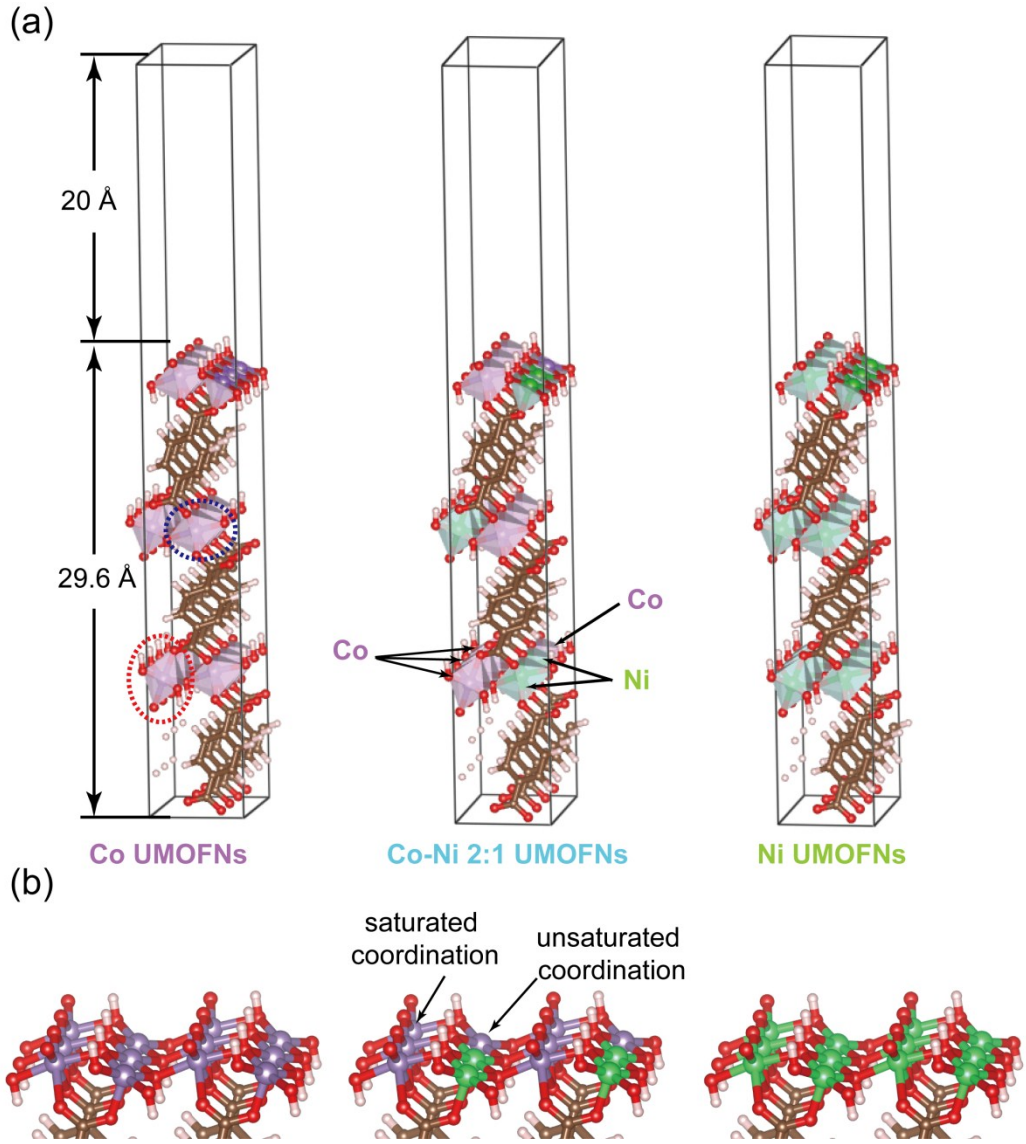

Figure S9. (a) The slab models and (b) surface configurations of Co UMOFNs (left), Co-Ni 2:1 UMOFNs (middle), and Ni UMOFNs (right). The brown, red, pink, purple and green balls represent carbon, oxygen, hydrogen, cobalt and nickel atoms respectively. The purple and green octahedrons symbolize six O-coordinating cobalt and nickel centered octahedrons.

The supercell employed in theoretical calculation consists of three periodic layer along the x acis (29.6 Å) and a vacuum layer (20 Å). In the crystal structure, there're two kinds of six O-coordinating metal centered octahedrons, due to the O atoms are from carboxylates and hydroxyls.[S4] In the first kind of octahedron (kind I, cycled in red in Figure 9a), the metal atom is coordinated by 4 carboxylate O and 2 hydroxyl O, while the metal atom in the other kind octahedron is coordinated by 2 carboxylate O

and 4 hydroxyl O (kind II, cycled in black in Figure 9a). As for the surface of the top layer adjoining the vacuum layer, owing to the termination of BDC ligands, some unsaturated coordinated metal atom may be produced. As revealed previously,[S4] the configurations in which the metal atom in kind I octahedron is saturated coordinated (6-coordinated) by carboxylate, hydroxyl, and adsorbed O, and the metal atom in kind II octahedron is unsaturated coordinated (5-coordinated) was the most satisfactory structural model (Figure S9b). So it was also used in our theoretical calculation. In the bimetallic UMOFNs, the Co or Ni atoms may locate in the center of two kinds of octahedrons. According to our calculations, the construction of Ni in kind II octahedron (also in the unsaturated coordinated sites) has the greatest thermodynamic stability. In summary, the crystal models and surface configurations of Co UMOFNs, Co-Ni 2:1 UMOFNs, and Ni UMOFNs are displayed in the left, middle and right parts of figure 9 respectively.

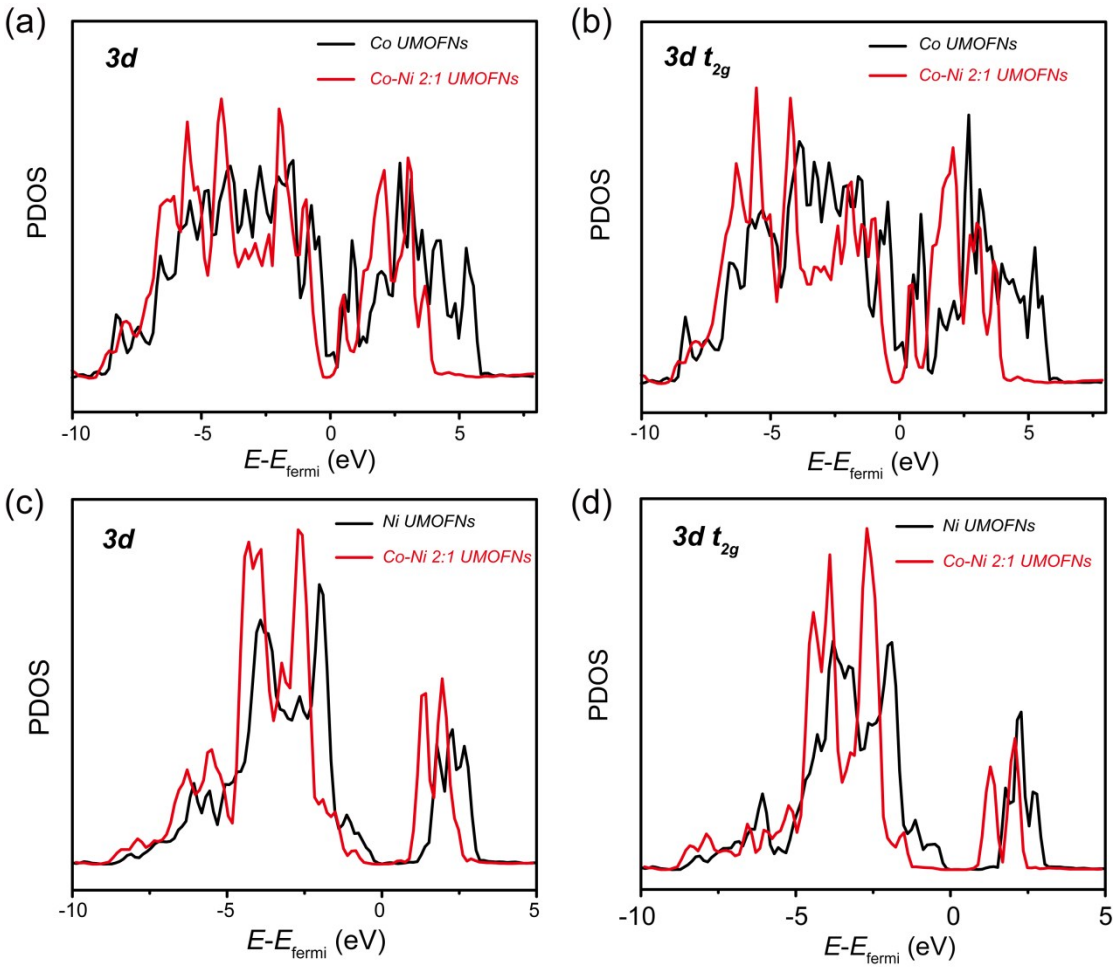

Figure S10. (a, b) PDOS profiles of Co 3d states (a) and 3d t_{2g} (b) in Co UMOFNs (black curve) and Co-Ni 2:1 UMOFNs (red curve). (c, d) PDOS profiles of Ni 3d states (c) and 3d t_{2g} states (d) in Ni UMOFNs (black curve) and CoNi 2:1 UMOFNs (red curve).

Table S2. The average charges of Co, Ni and O by bader charge analysis in Co UMOFNs, Ni UMOFNs and Co-Ni 2:1 UMOFNs.

Samples	Co	Ni	O
Co UMOFNs	1.311	\	- 1.109
Co-Ni 2:1 UMOFNs	1.234	1.252	- 1.144
Ni UMOFNs	\	1.243	- 1.163

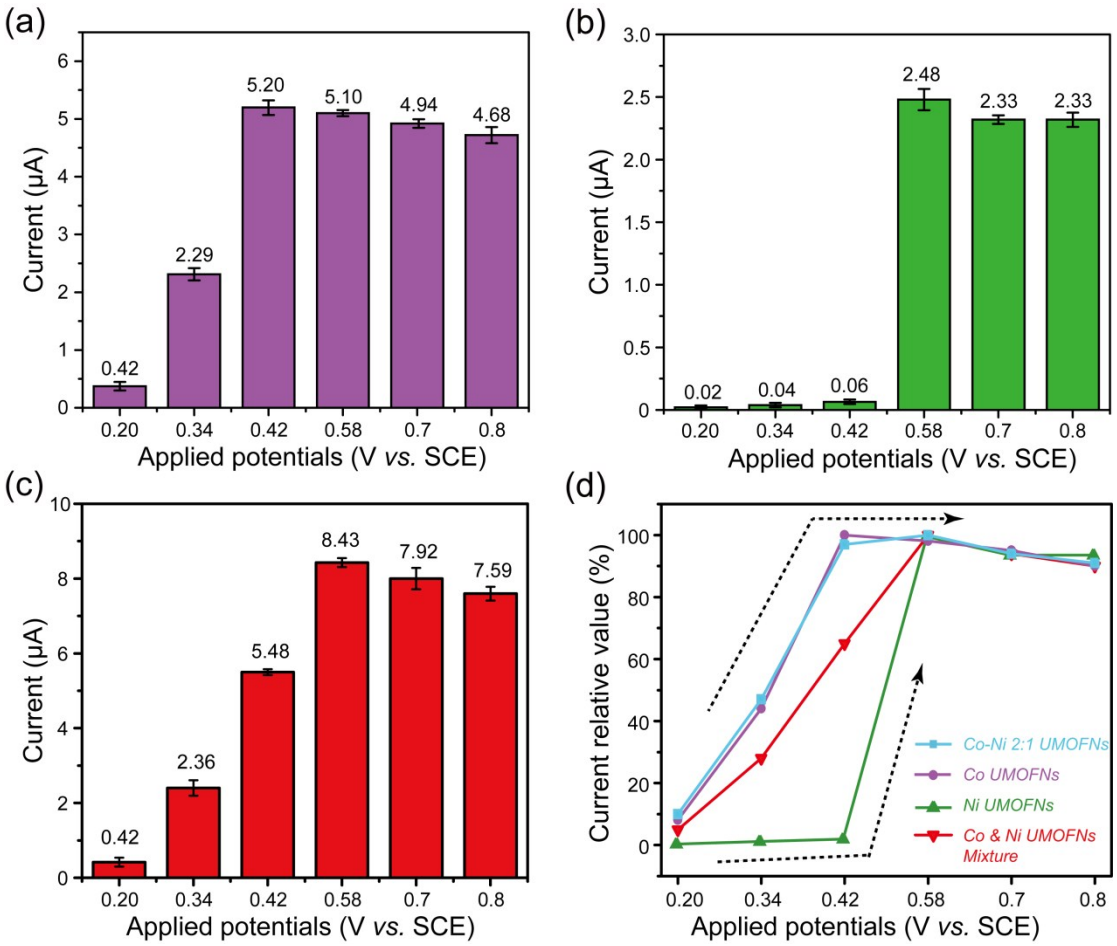

Figure S11. The current response intensity of Co UMOFNs (a), Ni UMOFNs (b) and Co and Ni UMOFNs mixture (c) towards 0.1 M glucose at different applied potentials. (d) The variation tendency of current relative value (vs. each maximum absolute current value of four UMOFNs, Co-Ni 2:1 UMOFNs: 35.25 μA; Co UMOFNs: 5.20 μA; Ni UMOFNs: 2.48 μA; Co and Ni UMOFNs mixture: 8.43μA) of four UMOFNs samples.

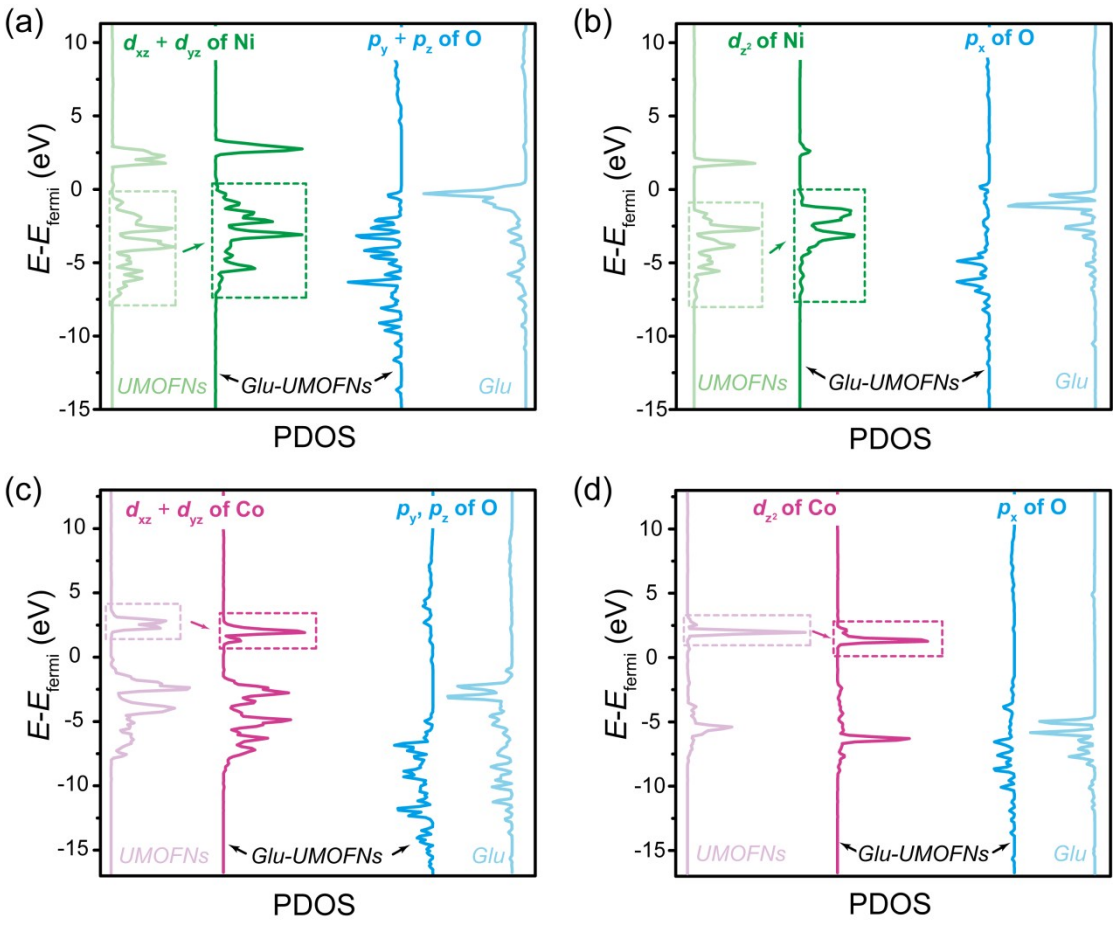

Figure S12. (a) PDOS profiles of t_{2g} states (d_{xz} + d_{yz} orbits, green curves, the same below) of Ni at adsorption site in Ni UMOFNs, and π bond (p_y + p_z orbits, blue curves, the same below) of adsorbed O in glucose before (two sides, the same below) and after (middle, the same below) glucose's adsorbtion. (b) PDOS profiles of e_g states (d_{z^2} orbits, green curves) of Ni, and σ bond (p_x orbits, blue curves) of adsorbed O before and after glucose's adsorbtion. (c) PDOS profiles of t_{2g} states of Co at adsorption site in Co UMOFNs, and π bond of adsorbed O in glucose before and after glucose's adsorbtion. (d) PDOS profiles of e_g states of Co, and σ bond of adsorbed O before and after glucose's adsorbtion.

For the UMOFUs, the unsaturated coordinated (5-coordinated) metal (Co or Ni) played the adsorbed site in the glucose' adsorption, which is the first step of electrochemical sensing based on the oxidation of glucose. The intensive bonding interaction between metal site and the adsorbing O atom in glucose is the basic of swift electron transfer from O to metal and the subsequent oxidation reaction. There're two bonding interactions between metal and the adsorbing O (Figure 4d), namely the bonding of t_{2g} orbits of metal (mainly made of d_{xz} and d_{yz} orbits) and π bond of O (mainly made of p_y and p_z orbits), and the bonding of e_g orbits of

metal (d_{z2} orbits) and σ bond of O (p_x orbits). The bonding interaction could make occupied orbitals states (bonding orbitals, below fermi level) shift to lower energy or unoccupied orbitals states (anti-bonding orbitals, above fermi level) to higher energy, which gives rise to the reduce in total energy of the adsorption configuration. Besides, the generation of new occupied or unoccupied orbital states has the same effect.

Learning from of PDOS of t_{2g}, e_g orbits of metal and π, σ bonds of adsorbed O after glucose adsorption (Figure 4 and S12), substantial changes reducing the total energy of the adsorption configuration occured (i.e. new bonding orbitals states generated or shift to lower energy et al.), demonstrating the strong bonding interaction between glucose and UMOFNs and potential excellent sensing property. Anyway, as shown in PDOS profiles glucose-adsorbed Ni UMOFNs slab (Figure S12a, b), both of t_{2g} and e_g bonding orbitals PODS of Ni exhibited a shift to higher energy (green inserted box in Figure S12a, b). And in the PDOS profiles glucose-adsorbed Co UMOFNs slab, both of t_{2g} and e_g anti-bonding orbitals PODS of Co gave a shift to lower energy (purple inserted box in Figure S12c, d). So it could be concluded that compared to the bimetallic Co-Ni 2:1 UMOFNs, the bonding interactions between glucose and monometallic UMOFNs was weaker than that for glucose-bimetallic UMOFNs. It was agreed by ΔE_{ads} of glucose on three UMOFNs, displayed in Table S3 below.

Table. S3 The adsorption energy (ΔE_{ads}, eV) of glucose on the slab model of Co UMOFNs, Ni UMOFNs and Co-Ni 2:1 UMOFNs.

Adsorbed site	Co UMOFNs	Co-Ni 2:1 UMOFNs	Ni UMOFNs
Co	- 0.40	- 0.50	\
Ni	\	- 1.26	- 1.02

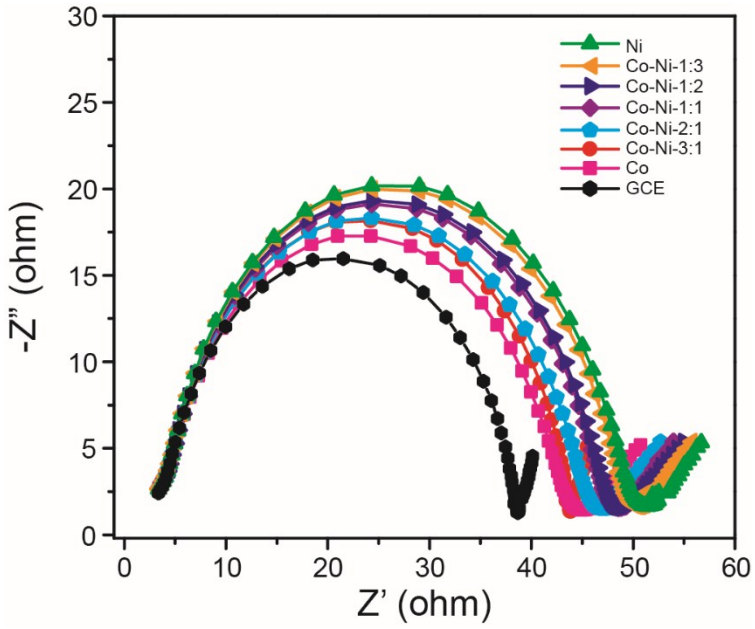

Figure S13. the electrochemical impedance spectroscopy (EIS) test for 7 different Co/Ni ratio UMOFNs (amplitude 5 mV; frequency range 0.1Hz to 10 kHz; 0.1M ferro/ferricyanide solution).

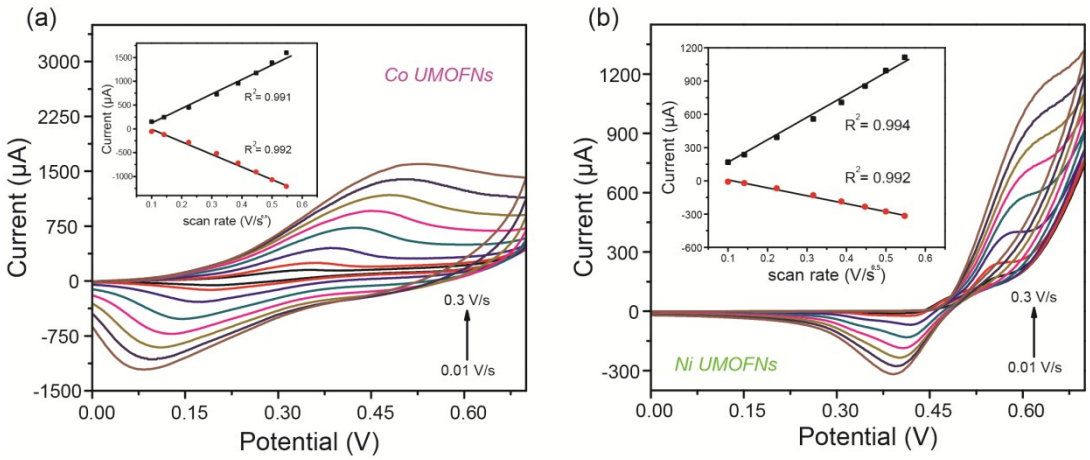

Figure S14. CV curves of the Co UMOFNs (a) and Ni UMOFNs (b) in 0.1M KOH electrolyte at different scan rates (0.01 - 0.3v/s). The inserts showed the linear fitting of anodic and cathodic peak current vs. sqrt scan rates.

Table S4. Glucose sensing performances of electrochemical sensor based on Co/Ni UMOFNs in seven different Co/Ni ratio, and Co UMOFNs + Ni UMOFNs (2:1) mixture.

Sample.	Sensetivity ($\mu A/mM/cm^2$)	Regression coefficient (R^2)	Linear region	Applied potential (V)
Co UMOFNs	321.2	0.9962	0.1 µM - 1 mM	0.43
Co-Ni 3:1 UMOFNs	697.4	0.9905	1 µM – 1 mM	0.42
Co-Ni 2:1 UMOFNs	2086.7	0.9968	0.1 µM – 1 mM	0.42
Co-Ni 1:1 UMOFNs	1212.4	0.9848	0.1 µM – 1.4 mM	0.42
Co-Ni 1:2 UMOFNs	606.9	0.9906	1 µM - 1 mM	0.42
Co-Ni 1:3 UMOFNs	216.6	0.9978	1 µM - 1 mM	0.42
Ni UMOFNs	173.1	0.9915	1 µM - 1 mM	0.58
Co/Ni UMOFNs mixture	373.5	0.9742	1 µM - 1 mM	0.42

Table S5. Glucose sensing performances of several non-enzymatic glucose sensors based on metal organic frameworks.

Electrode material	Sensitivity ($\mu A/mM/cm^2$)	Linear Range (µM)	Detection Limit (µM)	Ref.
MOF-$Ni(OH)_2/TiO_2$	192	Up to 14000	8	S5
CuO Nanoparticles	67.51	0-9680	1.01	S6
MOF-NiO/Foam Ni	395	18-1200	6.15	S7
Ni-MIL-77 (MOF)	1.542	1-500	0.25	S8
Au–CeO2	57.5	10-1000	10	S9
Co-MOF/NF	10886	0.001-3	0.0013	S10
MOF-$Co(OH)_2$/3DG	3690	0.1-10	0.016	S11
MOF-Co_3O_4	471.5	4-12.5	0.1	S12
CoOOH nanosheets	341	0.03-0.7	30.9	S13
Nano NiO	55.9	1-110	0.16	S14
Ni-rGO	813	1-110	55.9	S15
NiNPs/ATP/RGO	1414.4	1-710	0.37	S16
Co-Ni 2:1 UMOFNs	**2086.7**	**0.1-1400**	**0.047**	**This work**

Table S6. Table of electrode repeatability of Co-Ni 2:1 UMOFNs modified GCE glucose sensor (RSD is relative standard deviation).

No.	Sensitivity (μA/mM/cm^2)	RSD.
Electrode 1 (GCE)	2004.3	4.02%
Electrode 2 (GCE)	2194.2	5.12%
Electrode 3 (GCE)	2152.7	3.03%

Reference

S1 Y. Liang, R. Shang, J. Lu, L. Liu, J. Hu, W. Cui, *ACS Appl. Mater. Interfaces*, 2018, 10, 8758.

S2 F. Song, X. Hu, *Nat. Commun.*, 2014, 5, 4477.

S3 S. Storck, H. Bretinger, W. F. Maier, *Applied Catalysis A: General*, 1998, 174, 137.

S4 S. Zhao, Y. Wang, J. Dong, C.-T. He, H. Yin, P. An, K. Zhao, X. Zhang, C. Gao, L. Zhang, J. Lv, J. Wang, J. Zhang, A. M. Khattak, N. A. Khan, Z. Wei, J. Zhang, S. Liu, H. Zhao, Z. Tang, *Nat. Energy*, 2016, 1, 16184.

S5 A. Gao, X. Zhang, X. Peng, H. Wu, L. Bai, W. Jin, G. Wu, R. Hang, P. K. Chu, *Sens. Actuator B-Chem.*, 2016, 232, 150.

S6 J. Song, L. Xu, C. Zhou, R. Xing, Q. Dai, D. Liu, H. Song, *ACS Appl. Mater. Interfaces*, 2013, 5, 12928.

S7 L. Wang, Y. Xie, C. Wei, X. Lu, X. Li, Y. Song, *Electro. Acta.*, 2015, 174, 846.

S8 X. Xiao, S. Zheng, X. Li, G. Zhang, X. Guo, H. Xue, H. Pang, *J. Mat. Chem. B*, 2017, 5, 5234.

S9 M. Gougis, A. Pereira, D. Ma, M. Mohamedi, *RSC Adv.*, 2014, 4, 39955.

S10 Y. Li, M. Xie, X. Zhang, Q. Liu, D. Lin, C. Xu, F. Xie, X. Sun, *Sens. Actuator B-Chem.*, 2019, 278, 126.

S11 I. Shackery, U. Patil, A. Pezeshki, N. M. Shinde, S. Im, S. C. Jun, *Microchim. Acta*, 2016, 183, 2473.

S12 L. Han, D.-P. Yang, A. Liu, *Biosens. Bioelectron.*, 2015, 63, 145.

S13 K. K. Lee, P. Y. Loh, C. H. Sow, W. S. Chin, *Electrochem. Commun.*, 2012, 20, 128.

S14 Y. Mu, D. Jia, Y. He, Y. Miao, H.-L. Wu, *Biosens. Bioelectron.*, 2011, 26, 2948.

S15 Z. Wang, Y. Hu, W. Yang, M. Zhou, X. Hu, *Sensors*, 2012, 12, 4860.

S16 Z. Shen, W. Gao, P. Li, X. Wang, Q. Zheng, H. Wu, Y. Ma, W. Guan, S. Wu, Y. Yu, K. Ding, *Talanta*, 2016, 159, 194.